Electronic Supplementary Material (ESI) for Journal of Materials Chemistry A.
This journal is © The Royal Society of Chemistry 2024

Supplementary Information

Trifunctional Fe-based electrocatalyst with sturdy three-dimensional frame construction for ORR, OER and HER

Haixia Liang[a], Jian Li[b], Jinli Zhang[*a, c], Wencai Peng[*a], Jun Li[d], Jichang Liu[e]

[a] *School of Chemistry and Chemical Engineering, Shihezi University/ State Key Laboratory Incubation Base for Green Processing of Chemical Engineering, Shihezi 832003, Xinjiang, China.*

[b] *State Key Laboratory of Advanced Technologies for Comprehensive Utilization of Platinum Metals, Kunming Institute of Precious Metals, Kunming 650106, China.*

[c] *Key Laboratory for Systems Bioengineering MOE, Tianjin University; Collaborative Innovation Centre of Chemical Science and Chemical Engineering (Tianjin), Tianjin 300072, China.*

[d] *State Key Laboratory of Multiphase Complex Systems, Institute of Process Engineering, Chinese Academy of Sciences, Beijing 100190, China.*

[e] *State Key Laboratory of Chemical Engineering, East China University of Science and Technology, Shanghai 200237, China*

** Corresponding author: E-mail: pengwencai@shzu.edu.cn.*

** Corresponding author: E-mail: zhangjinli@tju.edu.cn.*

1. Experimental section

1.1 Materials characterization

The structures, morphologies and element composition were studied by Scanning electron microscopic (SEM, Hitachi SU8010, Japan) equipped with an EDX spectrometer and transmission electron microscopy (TEM, FEI Tecnai G2 F30, USA). X-ray diffraction (XRD) patterns were conducted on a Bruker D8 (Germany) apparatus with Cu-K α radiation. Raman spectra were collected under a laser excitation of 514 nm by a Raman microscope (Renishaw, England). N_2 adsorption/desorption isotherms were obtained on a micromeritics ASAP 2020 equipment (USA), and the specific surface area and pore size distribution were calculated. X-ray photoelectron spectroscopy (XPS) was performed using a PHI-5100 Versa Probe instrument. Fe 2p, C 1s and N 1s spectra were recorded and calibrated using the C 1s peak (284.8 eV). The etermination of absolute condtent of Fe in catalysts by inductively coupled plasma optical emission spectrometry (ICP-OES, Varian 725-ES). The X-ray absorption data at the Fe K-edge of the samples were recorded at room temperature in transmission mode using ion chambers (referenced samples) and fluorescence excitation mode using a Lytle detector (controlled samples) at beamline BL14W1 of the Shanghai Synchrotron Radiation Facility (SSRF). The station was operated with a Si (111) double crystal monochromator. During the measurement, the synchrotron was operated at 3.5 GeV and the current was between 150-210 mA. The data for each sample were calibrated with standard Fe metal foil. Data processing was performed using the program ATHENA. Extended X-ray absorption fine structure (EXAFS) spectra were fitted using the FEFF 6.0 code.

2. Electrochemical measurements

All electrochemical performance tests are performed at room temperature using a standard three-electrode test system (CHI 760E, Shanghai). The working electrode is a glassy carbon (GC) electrode rotating disk electrode (RDE, 3 mm in diameter). Saturated Ag/AgCl and Pt wires are reference and counter electrodes, respectively. According to the Nernst equation, all potentials in this paper are converted into standard

reversible hydrogen electrode (RHE):

$$E_{(RHE)}=E_{(Ag/AgCl)}+0.0592\ pH+0.197 \quad (1)$$

Catalyst ink preparation: In this work, 3 mg of the catalyst was dispersed in a mixed solution of 475 uL anhydrous ethanol and 25 uL Nafion and sonicated for 30 min to obtain a well-dispersed catalyst ink.

2.1 ORR performance measurements

Working electrode preparation: The glassy carbon (GC) electrodes were polished for further utilization. Then 3.6 uL of ink was transferred to the polished GC electrode and air-dried at room temperature. The loading of prepared catalysts was 0.3 $mg \cdot cm^{-2}$. Commercial Pt/C serve as the reference catalyst with loading of 0.2 $mg \cdot cm^{-2}$.

The electrolyte (0.1M KOH) was purified with pure N_2 or O_2 for at least 30min to obtain N_2 or O_2 saturated electrolyte, and then the ORR test was performed. In ORR experiments, cyclic voltammetry (CV) curves were obtained at a scan rate of 10 mV/s. By adjusting the rotation speed (400rpm-2500rpm), the linear sweep voltammetry (LSV) curves were recorded at a scan rate of 10 mV/s. To obtained electrochemical surface area (ECSA) of catalysts, the double-layer capacitance (C_{dl}) is calculated from the CV plots in the region from 1.1 to 1.2 V (vs. RHE) with the scan rates of 3, 5, 10, 15, 20 and 25 mV s^{-1}. The C_{dl} values can be fitted by plotting the $(J_{anodic} - J_{cathodic})/2$ at 1.15 V (vs. RHE) against various scan rates. The linear slope is the C_{dl}. The i-t curves of the catalysts at 0.85 V were collected to evaluate the stable durability of the catalysts. The methanol tolerance of the catalysts was evaluated by adding a certain amount of methanol solution to the O_2-saturated electrolyte by chronoamperometry.

The electron transfer number (n) is obtained from the LSV curve, using the Kutecky-Levich (K-L) equation:

$$\frac{1}{J}=\frac{1}{J_K}+\frac{1}{J_L}=\frac{1}{J_K}+\frac{1}{B\omega^{1/2}} \quad (2)$$

$$B = 0.62nFC_0D_0^{2/3}v^{-1/6} \quad (3)$$

Where J (mA cm^{-2}), J_L and J_K are the tested, diffusion-limiting and kinetic current densities, respectively. ω (rad s^{-1}) is the angular velocity of the RDE electrode, F

represents the Faraday constant (96, 485 C mol^{-1}), D_0 and C_0 are the O_2 diffusion coefficient (1.9×10^{-5} cm^2 s^{-1}) and O_2 concentration (1.2×10^{-6} mol cm^{-3}) in 0.1 M KOH, respectively, v is the kinematic viscosity of the electrolyte (0.01 cm^2 s^{-1}).

2.2 OER and HER performance measurements

Working electrode preparation: The nickel foam is cut to size 1cm × 1cm and sonicated in acetone, ethanol and water solutions, respectively. Then a certain amount of catalyst ink was loaded onto a nickel foam and air dried naturally. All catalysts were loaded at 1 mg cm^{-2}. Pt/C and RuO_2 were loaded at the same 1 mg cm^{-2} as the baseline catalysts.

The electrocatalytic activity was examined by measuring the LSV curves in 1 M KOH solution with a scan rate of 10 mV s^{-1}. The electrochemical impedance spectroscopy (EIS) measurement was recorded in the frequency range of 0.01−100,000 Hz with an amplitude of 5 mV. The CP curve was collected at potential at 10 mA cm^{-2} to evaluate the durability of catalysts.

2.3 Zn-air batteries assembly

Polished zinc plates (thickness 0.3 mm) and air electrodes (including catalytic active layer and gas diffusion layer) were used as anode and cathode, respectively. The catalytically active layer was mixed with catalyst powder (3 mg), Nafion (20 μL) and ethanol solution (480 mL) by sonication for 60 min, then dropped into nickel foam (1 cm × 1 cm) and dried at room temperature. The catalytically active layer was then laminated to the nickel foam. For comparison, a hybrid catalyst of commercial Pt/C (1 mg) and RuO_2 (1 mg), labeled as Pt/C+RuO_2, was also prepared. The electrolyte was 6 M KOH. All catalysts were loaded at 2 mg cm^{-2}.

2.4 Overall water splitting device

A two-electrode water splitting device was assembled using Fe_3C-Fe/NC-800 as a bifunctional electrocatalyst for both OER and HER. The Fe_3C-Fe/NC-800 electrocatalyst was fully and uniformly coated on the nickel foam (1 cm × 1 cm) to furnish the electrode with the electrocatalyst loading of 1 mg cm^{-2}.

The electrocatalytic activity was examined by measuring the LSV curve in 1 M KOH

solution with a scan rate of 10 mV s^{-1}. The CP curve was collected at potential at 10 mA cm^{-2} to evaluate the durability of catalysts.

2.5 Density functional theory details

All DFT calculations were carried out by the Vienna ab initio Simulation Package (VASP)[1, 2]. The Perdew-Burke-Ernzerhof (PBE)[3] exchange-correlation functional and projector augmented wave (PAW)[4] pseudopotential were adopted with spin-polarization. During the structure optimization, the convergence criterion of total energy was set to 10^{-6} eV, and the atoms were relaxed until the force acting on each atom was less than 0.01 eV/Å. Gaussian smearing of 0.05 eV to the orbital occupation is applied. A plane-wave cut-off energy of 450 eV was used in all computations. The Brillouin-zone integrations were conducted using Monkhorst-Pack (MP) grids of special points with the separation of 0.06 $Å^{-1}$. Each slab model was separated from its neighbors by 15 Å vacuum layer spacing. DFT-D3 method of Grimme with zero-damping function were used in van der Waals (vdW) corrections. The free energy profiles, which are efficient in estimating the performance of electrocatalytic reactions, were acquired by applying the computational electrode model (CHE)[5].

The Gibbs free energies of the ORR were calculated by correcting the DFT energy with zero-point energy and entropy via:

$$\Delta G = \Delta E + \Delta ZPE - T\Delta S \quad (4)$$

where E is the DFT total energy, ZPE is the zero-point energy, T is the environmental temperature, and S is the entropy. For zero-point energy correction and entropy calculations, the vibrational frequencies were calculated by employing density functional perturbation theory.

The theoretical model of Fe_3C-Fe/NC-800, consisting of monatomic FeN_4 and Fe_3C (031) facets, was constructed based on the results of XRD, HRTEM, XPS, and EXAFS characterisation, and ORR, OER, and HER DFT calculations were performed. The experimental results are combined with the DFT calculations for the investigation of the reaction mechanism.

The process of ORR reaction of Fe_3C-Fe/NC-800 in alkaline media can be divided into the following 4 elementary steps:

(1) $* + O_2\,(g) + H_2O\,(l) + e^- \rightarrow *OOH + OH^-$

(2) $*OOH + e^- \rightarrow *O + OH^-$

(3) $*O + H_2O\,(l) + e^- \rightarrow *OH + OH^-$

(4) $*OH + e^- \rightarrow * + OH^-$

where * indicates the active site or state.

Captions of Figures and Tables

Figure S1 SEM images of (a) Fe_3C-Fe/NC-700, (b) Fe_3C-Fe/NC-900, (c) SiO_2 and (d) HM-800.

Figure S2 XRD of Fe_3C-Fe/NC-800 and HM-800.

Figure S3 (a) N_2 adsorption and desorption isotherms and (b) pore size distribution of Fe_3C-Fe/NC-700, Fe_3C-Fe/NC-800 and Fe_3C-Fe/NC-900.

Figure S4 XPS spectra of Fe_3C-Fe/NC-800 and HM-800.

Figure S5 (a) The high-resolution XPS spectra of O 1s and (b) EPR spectra for Fe_3C-Fe/NC-800.

Figure S6 The fitting of FT-EXAFS spectra for Fe3C-Fe/NC-800 (a and b), Fe Foil (c and d) and FePc (e and f) at k and R space.

Figure S7 CV curves of Fe_3C-Fe/NC-800 in N_2-saturated and O_2-saturated (a), CV curves of Fe_3C-Fe/NC-800, HM-800 and SiO_2 in O_2-saturated in 0.1 M KOH electrolyte.

Figure S8 Tafel plots of Fe_3C-Fe/NC-800, HM-800, SiO_2 and Pt/C in 0.1 M KOH for ORR.

Figure S9 LSV curves of Fe_3C-Fe/NC-800 (a), HM-800 (c) and SiO_2 (e) at various electrode rotation rates (400-2500 rpm), K-L plots and electron transfer number (n) of Fe_3C-Fe/NC-800 (b), HM-800 (d) and SiO_2 (f).

Figure S10 Electrochemical cyclic voltammetry curves for Fe_3C-Fe/NC-800 (a), HM-800 (b) and SiO_2 (c) and Pt/C (d) at different scan rates in O_2-saturated 0.1 M KOH. Plot of capacitive currents density (j_{anodic} - $j_{cathodic}$) of Fe_3C-Fe/NC-800, HM-800, SiO_2 and Pt/C electrodes at 1.10 V vs RHE as a function of various scan rates.

Figure S11 ORR polarization curves of Fe_3C-Fe/NC-800 recorded in O_2 saturated 0.1 M KOH with and without poisoning by 10 Mm SCN^-.

Figure S12 Current–time curves before and after the injection of methanol for Fe_3C-Fe/NC-800 and Pt/C.

Figure S13 LSV curves of Fe_3C-Fe/NC-800 and Pt/C before and after i-t test of ORR stability test.

Figure S14 (a, b) SEM images of Fe_3C-Fe/NC-800 after i-t test for ORR stability test at 0.85 V and 400 rpm.

Figure S15 Nyquist plots of Fe_3C-Fe/NC-800, HM-800 and RuO_2 for OER.

Figure S16 LSV curves of Fe_3C-Fe/NC-800 before and after CP test of OER stability test.

Figure S17 The overall LSV curve of ORR and OER bifunctional activities for Fe_3C-Fe/NC-800 in

O_2-saturated 0.1 M KOH at a rotation rate of 1600 rpm.

Figure S18 Nyquist plots of Fe_3C-Fe/NC-800, HM-800 and Pt/C for HER.

Figure S19 LSV curves of Fe_3C-Fe/NC-800 before and after CP test of HER stability test.

Figure S20 SEM images and EDX spectra of Fe_3C-Fe/NC-800 (a) before and (b) after CP test for HER stability test.

Figure S21 Specific capacity of Fe_3C-Fe/NC-800 and Pt/C+RuO_2 based Zn-air batteries at 10 mA cm^{-2}.

Figure S22 LSV curves of Fe_3C-Fe/NC-800 before and after CP test of overall water splitting stability test.

Figure S23 H_2 and O_2 volumes of Fe3C-Fe/NC-800 (+||-) electrode at a fixed current density of 50 mA cm^{-2}.

Figure S24 The optimized structures of the intermediates of the ORR on (a) FeN_4 and (b) Fe_3C.

Figure S25 Structural optimisation of H* adsorbed on (a) FeN_4/Fe_3C, (b) FeN_4 and (c) Fe_3C for HER.

Table S1 Surface atom contents of samples from XPS.

Table S2 The concentration of each N configuration in different samples from XPS.

Table S3 EXAFS fitting parameters at the Fe K-edge for various samples.

Table S4 $E_{1/2}$, overpotential and Tafel slopes of the prepared catalysts, Pt/C and RuO_2.

Table S5 Simulated R_s and R_{ct} value of Fe_3C-Fe/NC-800, RuO_2 and HM-800 for OER.

Table S6 Simulated R_s and R_{ct} value of Fe_3C-Fe/NC-800, Pt/C and HM-800 for HER.

Table S7 Summary of ORR, OER and HER performances of reported multifunctional electrocatalysts in recent open literatures.

Table S8 Total number of spectra of distribution maps before HER stability test.

Table S9 Total number of spectra of distribution maps after HER stability test.

Table S10 Comparison of the performance of Fe_3C-Fe/NC-800 with other reported catalysts for Zn-air batteries.

Table S11 Comparison of the performance of Fe_3C-Fe/NC-800 with other reported catalysts for overall water splitting.

Table S12 ΔG of ORR from DFT calculations.

Supplementary Figures

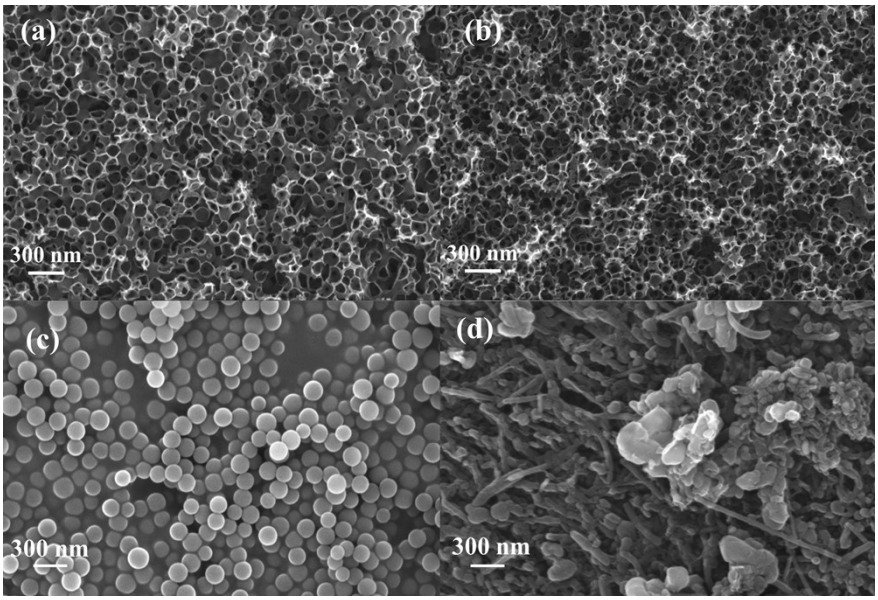

Figure S1 SEM images of (a) Fe_3C-Fe/NC-700, (b) Fe_3C-Fe/NC-900, (c) SiO_2 and (d) HM-800.

According to the SEM images, the catalysts Fe_3C-Fe/NC-700 and Fe_3C-Fe/NC-900 also had interconnected honeycomb structures, and when the calcination temperature was 900 °C, it was observed that part of the honeycomb structure on the surface of the catalyst Fe_3C-Fe/NC-900 was disrupted, which suggests that the appropriate calcination temperature helps to retain honeycomb structures.

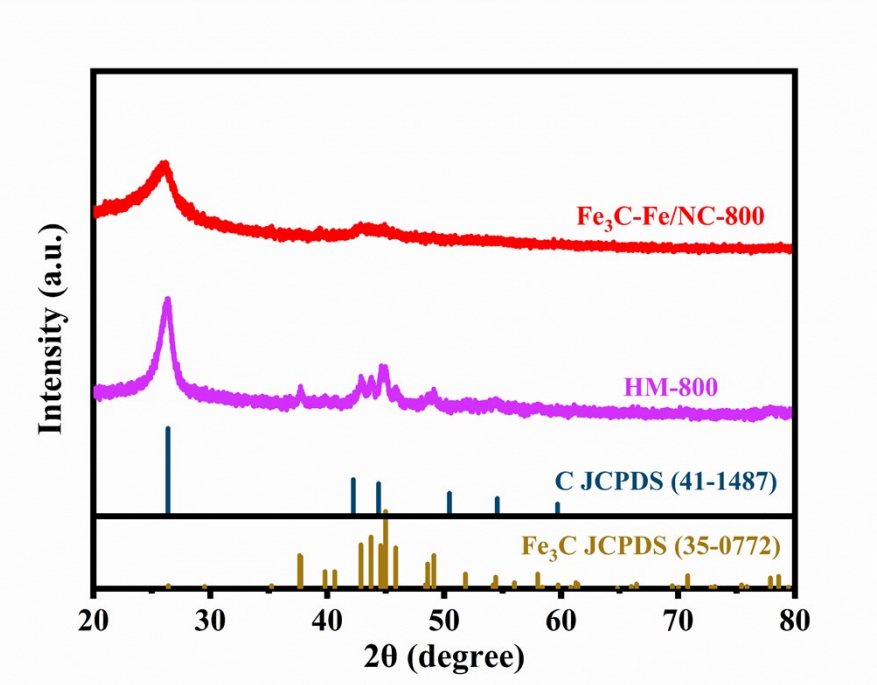

Figure S2 XRD of Fe_3C-Fe/NC-800 and HM-800.

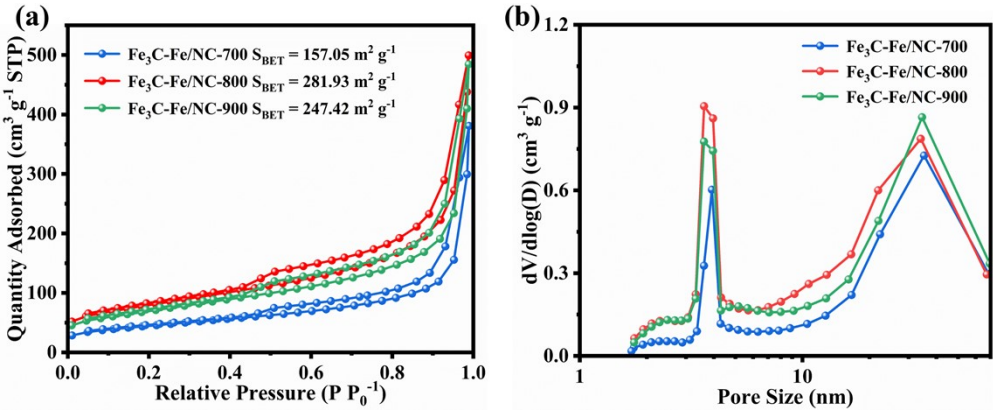

Figure S3 (a) N_2 adsorption and desorption isotherms and (b) pore size distribution of Fe_3C-Fe/NC-700, Fe_3C-Fe/NC-800 and Fe_3C-Fe/NC-900.

According to the N_2 adsorption desorption curves, the catalysts at different calcination temperatures have typical type IV isotherm type. This indicates the presence of a large number of mesoporous structures in the prepared catalysts. The pore size distribution shows small and large mesopores centred around at 3.6 nm and 34 nm. And it can be seen that Fe_3C-Fe/NC-900 has more large mesoporous structures from Figure S1b, which is consistent with the SEM results. The specific surface area of Fe_3C-Fe/NC-800 was 281.93 m^2 g^{-1}, which was larger than that of Fe_3C-Fe/NC-700 (157.05 m^2 g^{-1}) and Fe_3C-Fe/NC-900 (247.42 m^2 g^{-1}), suggesting that the carbonisation temperature also has effect on the specific surface area of the material. Therefore, suitable carbonisation temperature is more conducive to the generation of a larger specific surface area, allowing more active sites to be exposed[6, 7].

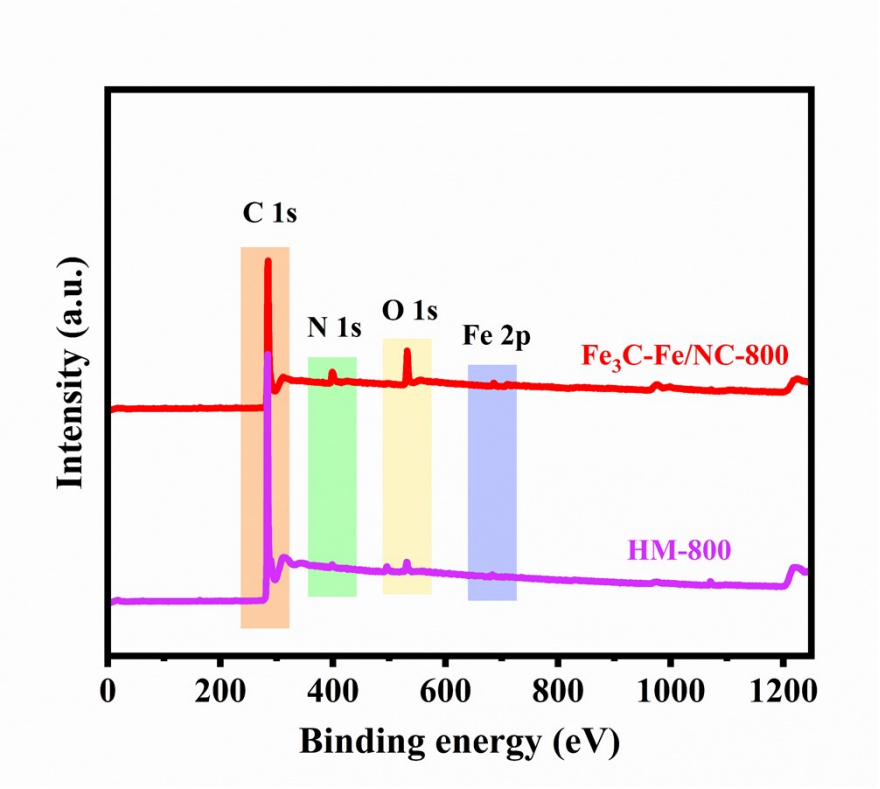

Figure S4 XPS spectra of Fe_3C-Fe/NC-800 and HM-800.

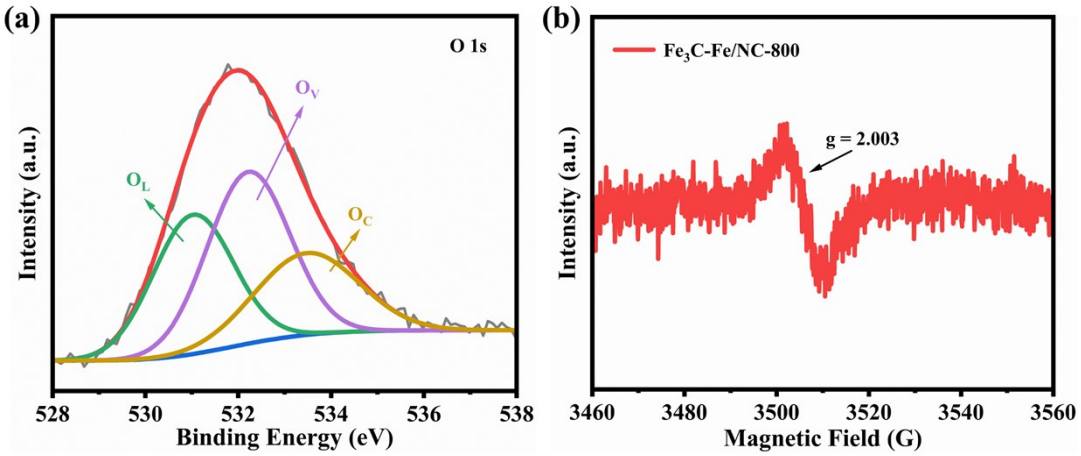

Figure S5 (a) The high-resolution XPS spectra of O 1s and (b) EPR spectra for Fe_3C-Fe/NC-800.

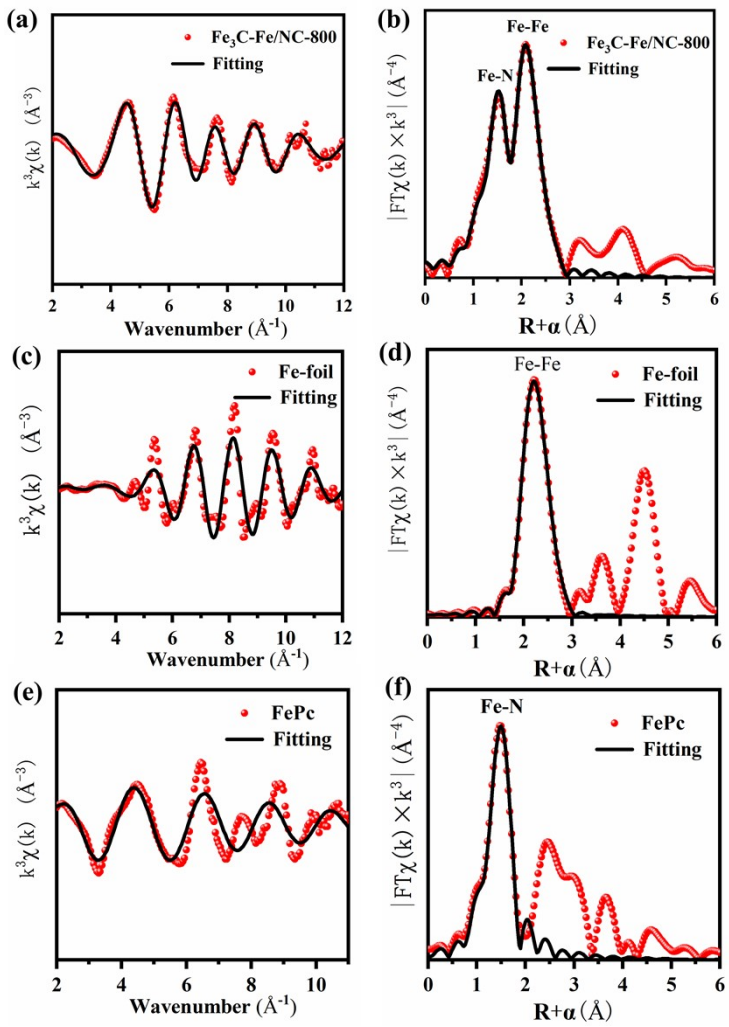

Figure S6 The fitting of FT-EXAFS spectra for Fe_3C-Fe/NC-800 (a and b), Fe Foil (c and d) and FePc (e and f) at k and R space.

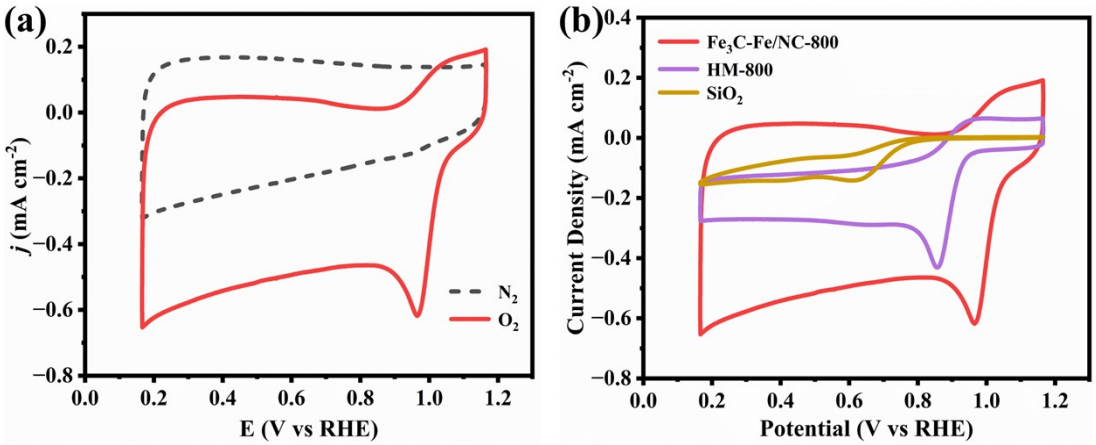

Figure S7 CV curves of Fe_3C-Fe/NC-800 in N_2-saturated and O_2-saturated (a), CV curves of Fe_3C-Fe/NC-800, HM-800 and SiO_2 in O_2-saturated in 0.1 M KOH electrolyte.

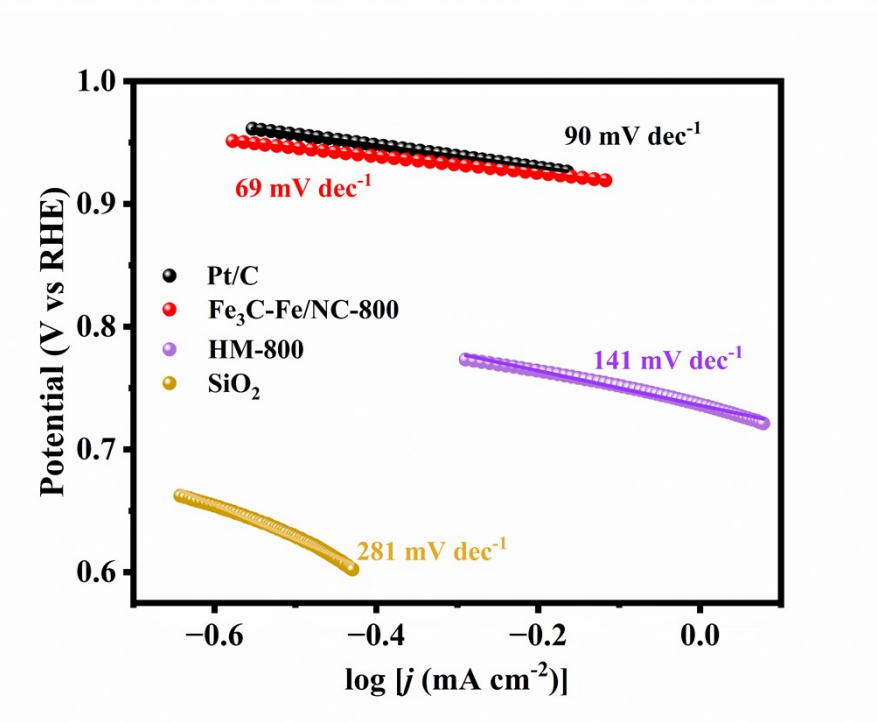

Figure S8 Tafel plots of Fe_3C-Fe/NC-800, HM-800, SiO_2 and Pt/C in 0.1 M KOH for ORR.

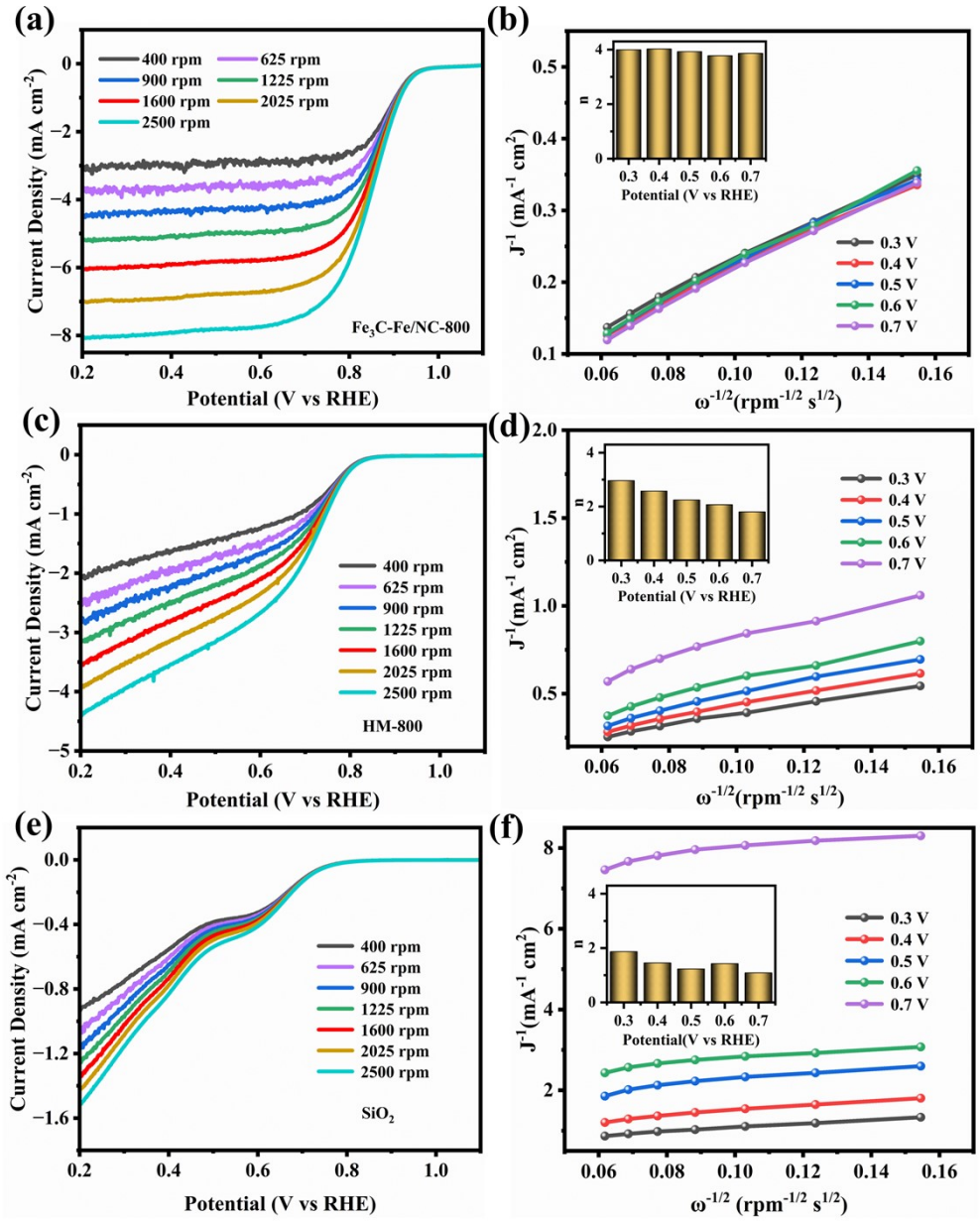

Figure S9 LSV curves of Fe_3C-Fe/NC-800 (a), HM-800 (c) and SiO_2 (e) at various electrode rotation rates (400-2500 rpm), K-L plots and electron transfer number (n) of Fe_3C-Fe/NC-800 (b), HM-800 (d) and SiO_2 (f).

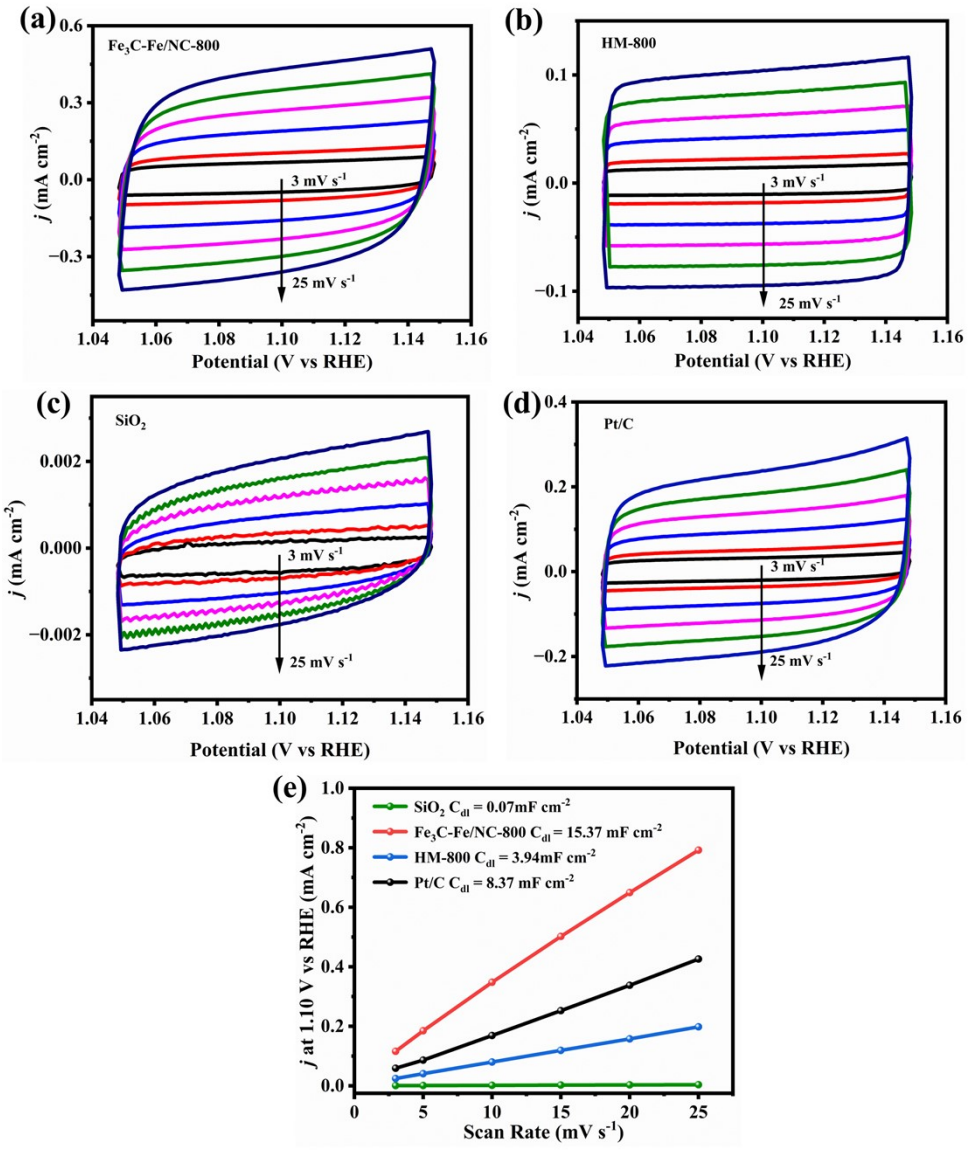

Figure S10 Electrochemical cyclic voltammetry curves for Fe_3C-Fe/NC-800 (a), HM-800 (b) and SiO_2 (c) and Pt/C (d) at different scan rates in O_2-saturated 0.1 M KOH. Plot of capacitive currents density (j_{anodic} - $j_{cathodic}$) of Fe_3C-Fe/NC-800, HM-800, SiO_2 and Pt/C electrodes at 1.10 V vs RHE as a function of various scan rates.

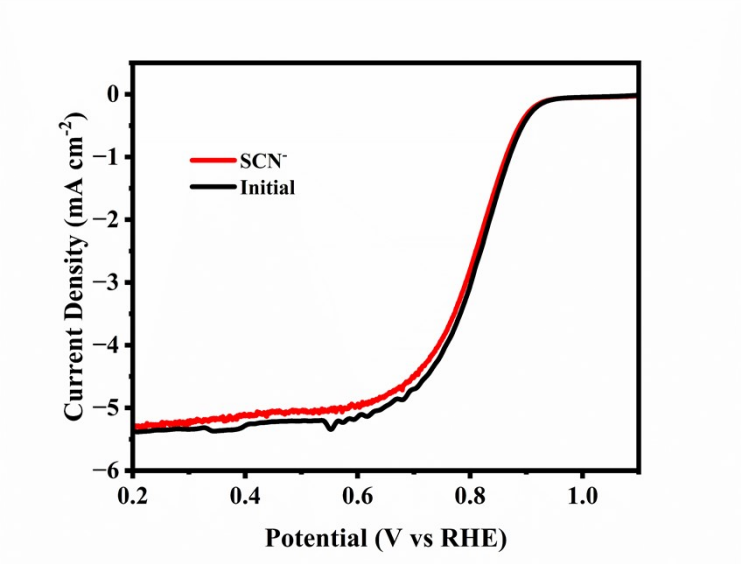

Figure S11 ORR polarization curves of Fe_3C-Fe/NC-800 recorded in O_2 saturated 0.1 M KOH with and without poisoning by 10 Mm SCN^-.

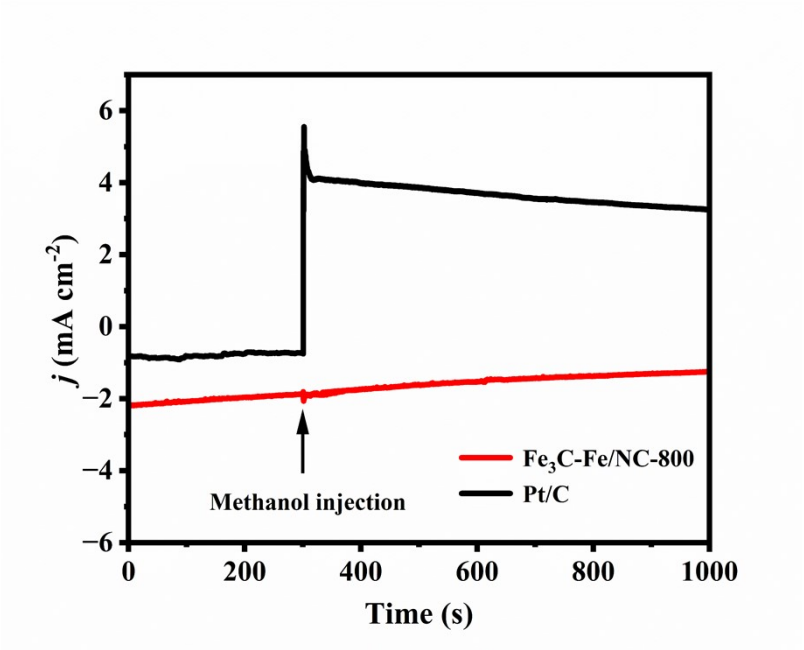

Figure S12 Current–time curves before and after the injection of methanol for Fe_3C-Fe/NC-800 and Pt/C.

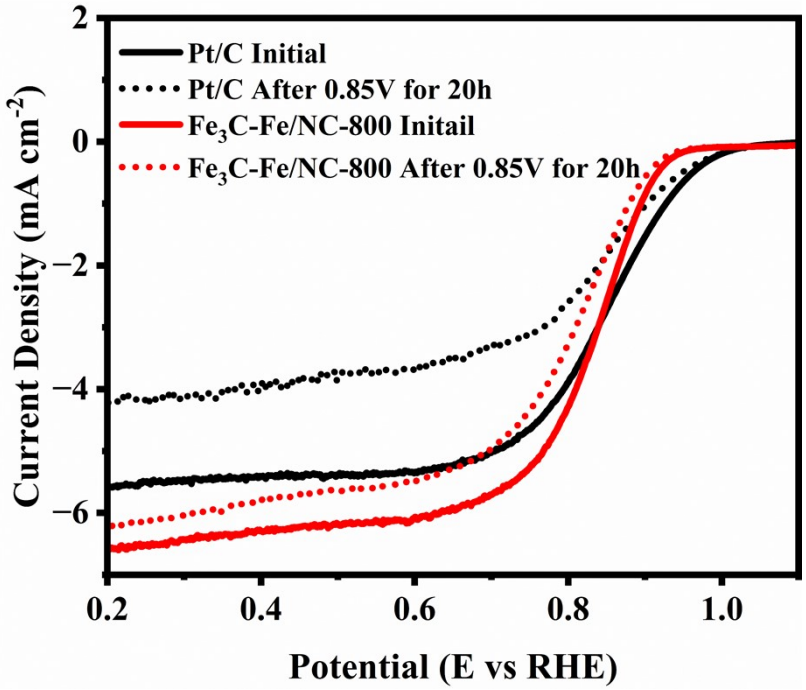

Figure S13 LSV curves of Fe_3C-Fe/NC-800 and Pt/C before and after i-t test of ORR stability test.

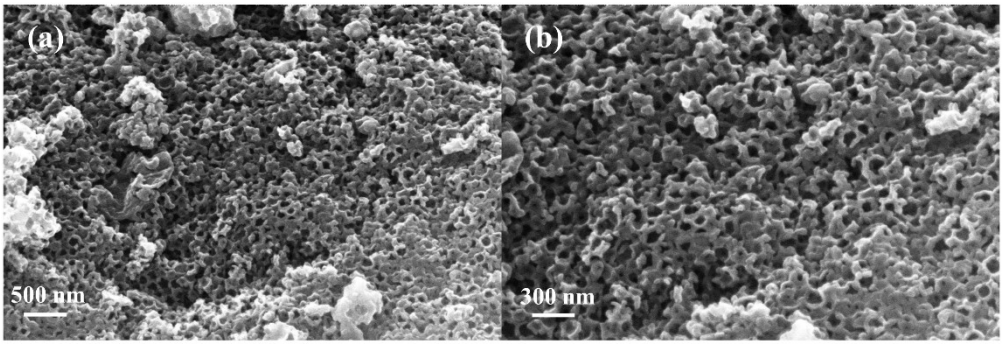

Figure S14 (a, b) SEM images of Fe_3C-Fe/NC-800 after i-t test for ORR stability test at 0.85 V and 400 rpm.

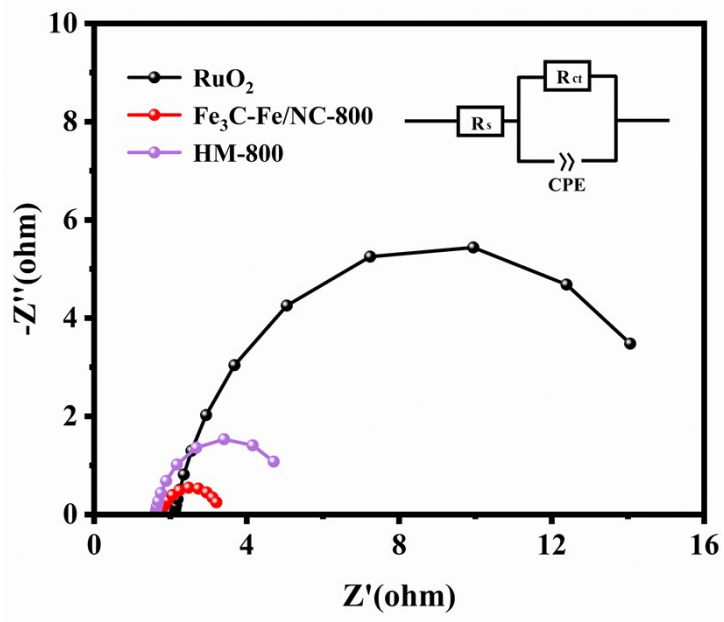

Figure S15 Nyquist plots of Fe_3C-Fe/NC-800, HM-800 and RuO_2 for OER.

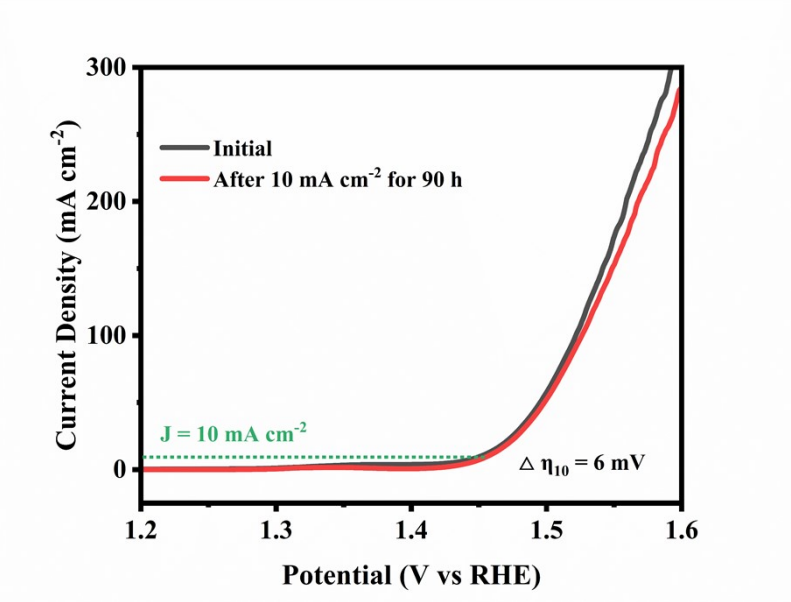

Figure S16 LSV curves of Fe_3C-Fe/NC-800 before and after CP test of OER stability test.

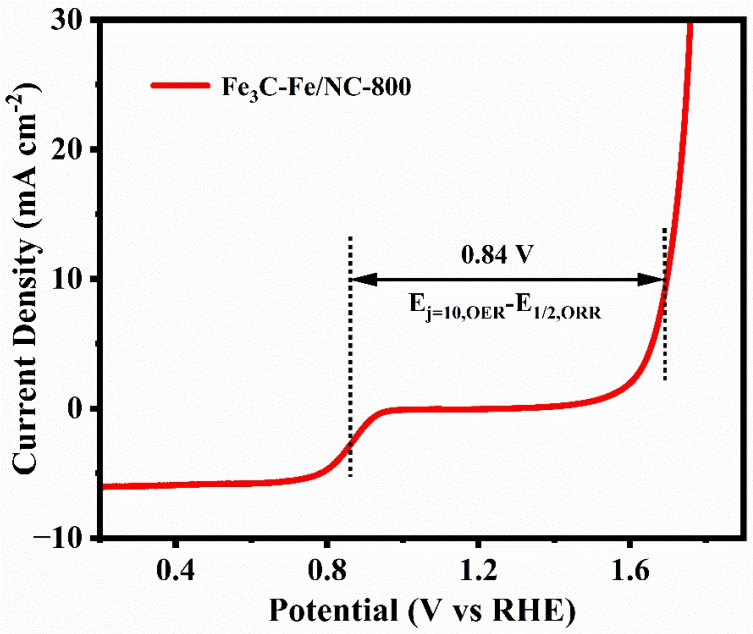

Figure S17 The overall LSV curve of ORR and OER bifunctional activities for Fe_3C-Fe/NC-800 in O_2-saturated 0.1 M KOH at a rotation rate of 1600 rpm.

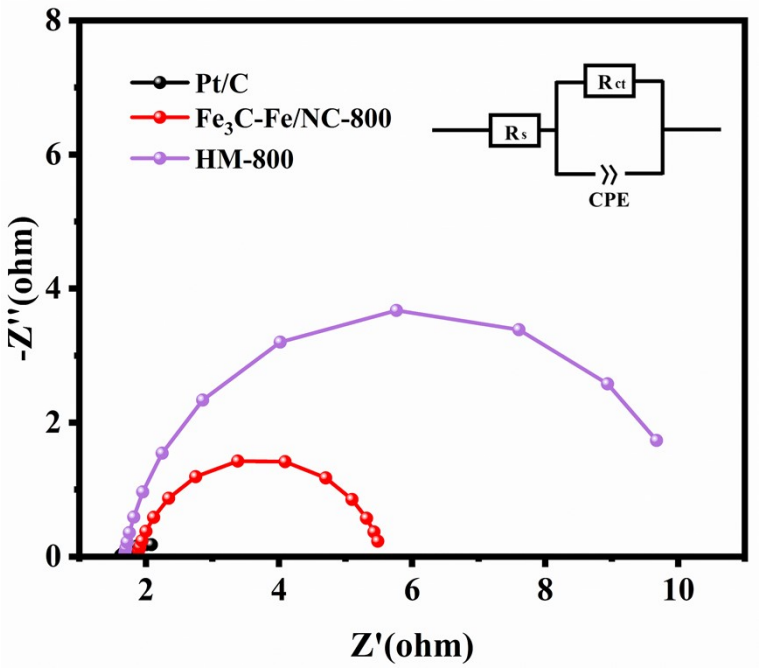

Figure S18 Nyquist plots of Fe_3C-Fe/NC-800, HM-800 and Pt/C for HER.

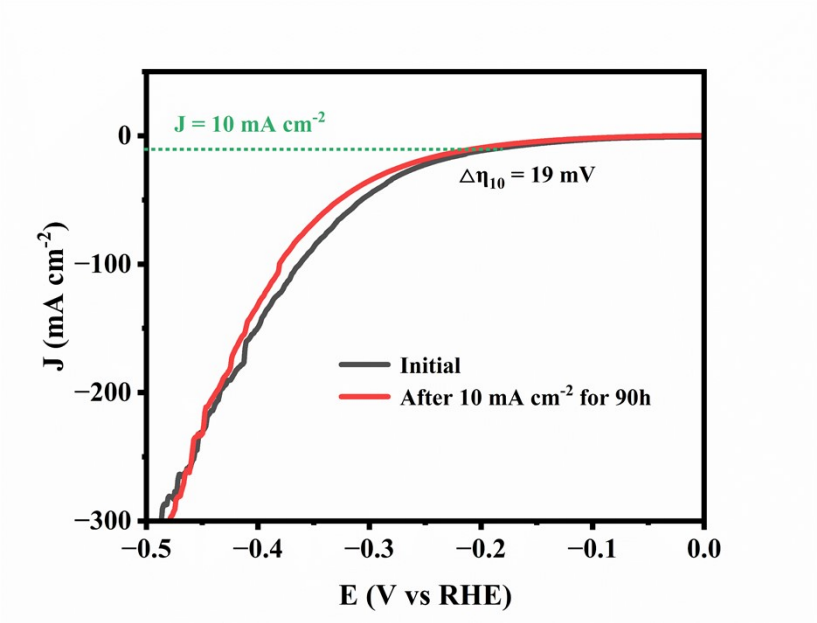

Figure S19 LSV curves of Fe_3C-Fe/NC-800 before and after CP test of HER stability test.

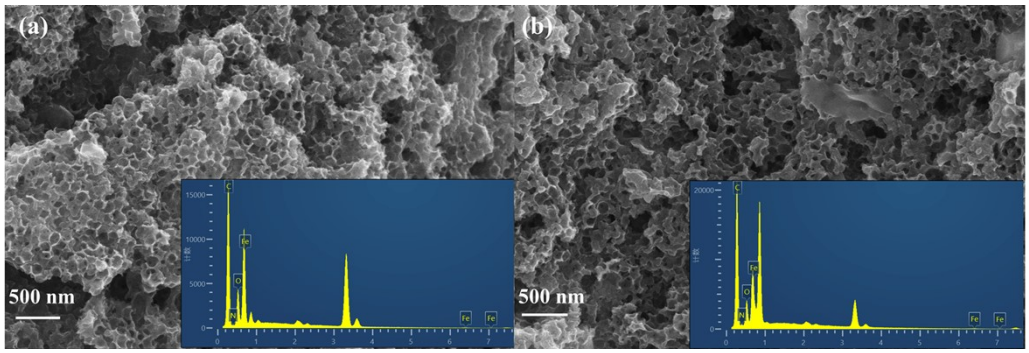

Figure S20 SEM images and EDX spectra of Fe_3C-Fe/NC-800 (a) before and (b) after CP test for HER stability test.

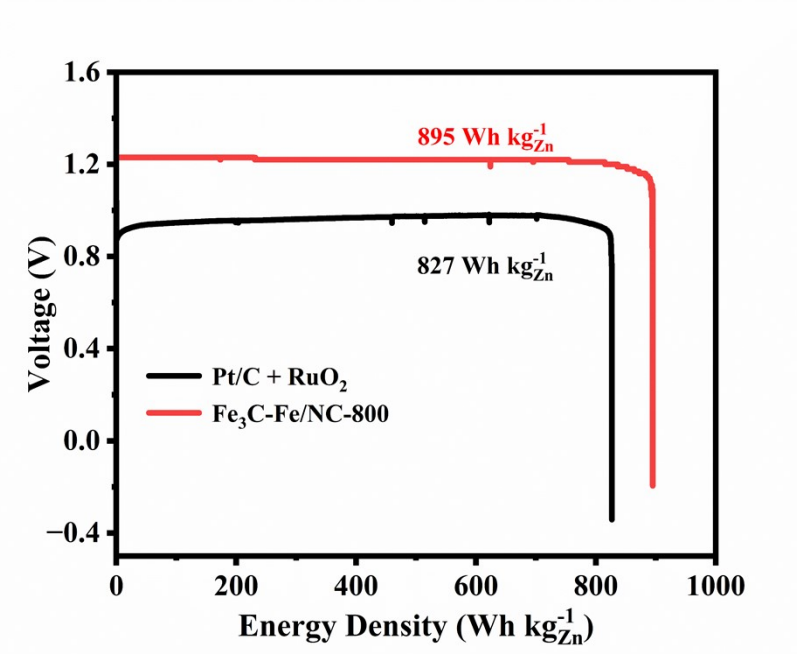

Figure S21 Energy Density of Fe_3C-Fe/NC-800 and Pt/C+RuO_2 based Zn-air batteries at 10 mA cm^{-2}.

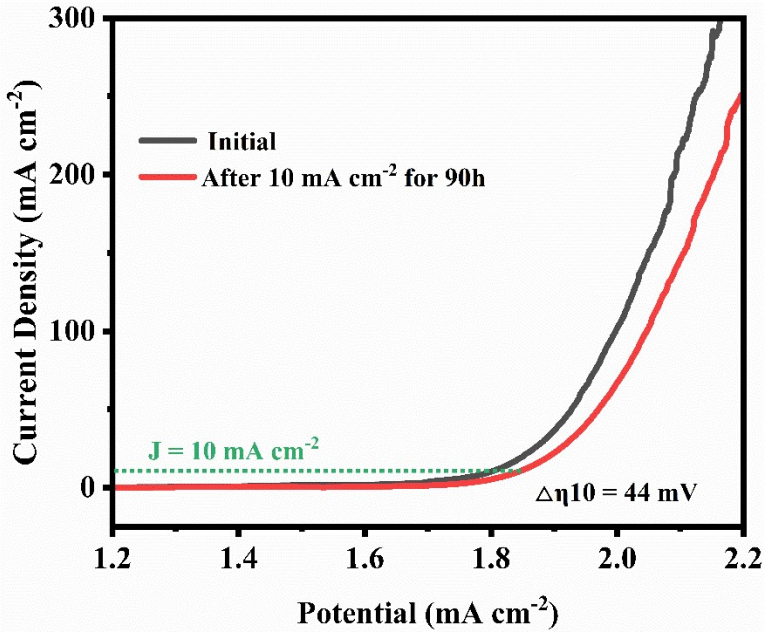

Figure S22 LSV curves of Fe_3C-Fe/NC-800 before and after CP test of overall water splitting stability test.

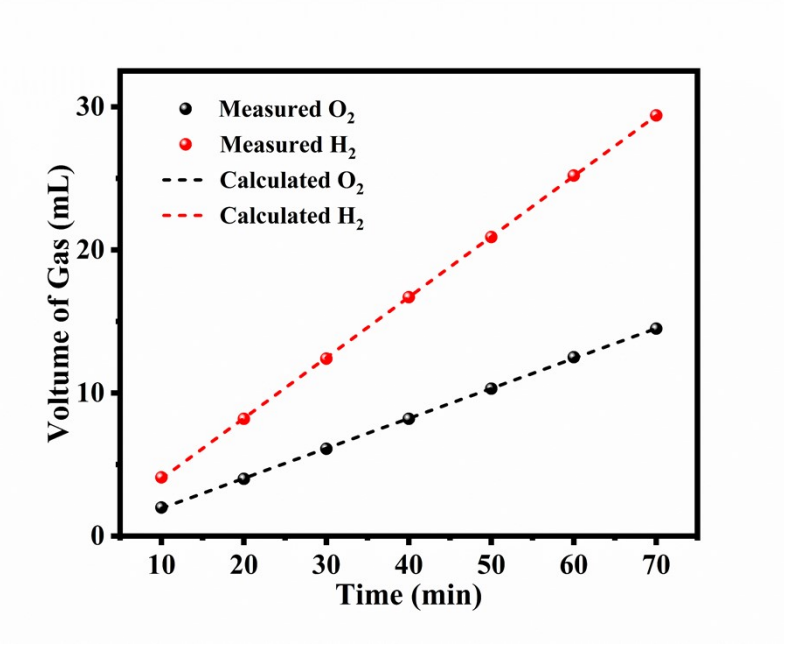

Figure S23 H_2 and O_2 volumes of Fe_3C-Fe/NC-800 (+||-) electrode at a fixed current density of 50 mA cm^{-2}.

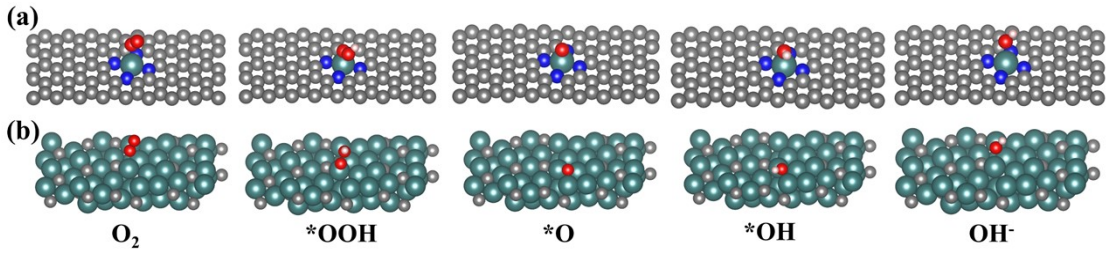

Figure S24 The optimized structures of the intermediates of the ORR on (a) Fe-N_4 and (b) Fe_3C.

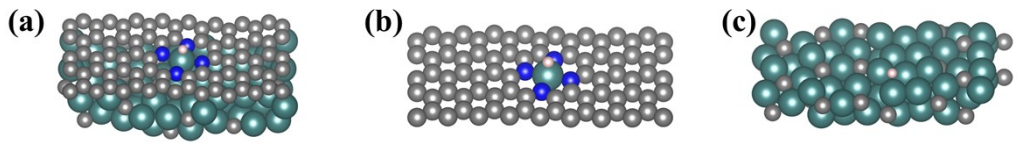

Figure S25 Structural optimisation of H* adsorbed on (a) Fe_3C/Fe-N_4, (b) Fe-N_4 and (c) Fe_3C for HER.

Supplementary Tables

Table S1 Surface atom contents of samples from XPS.

Sample	C 1s (at. %)	N 1s (at. %)	Fe 2p (at. %)	O 1s (at. %)
Fe_3C-Fe/NC-800	93.01	2.46	0.12	4.41
HM-800	97.48	1.05	0.15	1.32

Table S2 The concentration of each N configuration in different samples from XPS.

Sample / N type	Pyridinic-N (%)	Fe-Nx (%)	Pyrrolic-N (%)	Graphitic-N (%)	Oxidized-N (%)
Fe_3C-Fe/NC-800	28.23	17.21	19.26	15.98	19.32
HM-800	37.90	24.97	14.28	12.78	10.07

Table S3 EXAFS fitting parameters at the Fe K-edge for various samples.

sample	Shell	*CN*[a]	*R*(Å)[b]	σ^2(Å^2)[c]	ΔE_0(eV)[d]	*R* factor
Fe-foil	Fe-Fe	8*	2.467±0.012	0.0049±0.0013	6.0±2.0	0.0065
	Fe-Fe	6*	2.845±0.019	0.0056±0.0021	5.4±3.3	
FePc	Fe-N	4.0±0.3	1.970±0.001	0.0106±0.0029	0.6±0.5	0.0093
Fe_3C-Fe/NC-800	Fe-N	4.6±0.3	2.050±0.001	0.0064±0.0012	-1.4±0.4	0.0042
	Fe-Fe	2.2±0.3	2.585±0.001	0.0085±0.0014	1.1±0.7	
	Fe-Fe	4.8±0.7	3.119±0.007			

[a]*CN*, coordination number; [b]*R*, the distance to the neighboring atom; [c]σ^2, the Mean Square Relative Displacement (MSRD); [d]ΔE_0, inner potential correction; *R* factor indicates the goodness of the fit. $S0^2$ was fixed to 0.723, according to the experimental EXAFS fit of Fe foil by fixing *CN* as the known crystallographic value. * This value was fixed during EXAFS fitting, based on the known structure of Fe. Fitting range: $3.0 \leq k$ (/Å) ≤ 13.0 and $1.0 \leq R$ (Å) ≤ 3.0 (Fe foil); $2.0 \leq k$ (/Å) ≤ 11.0 and $1.0 \leq R$ (Å) ≤ 2.0 (FePc); $3.0 \leq k$ (/Å) ≤ 12.0 and $1.0 \leq R$ (Å) ≤ 2.9 (Fe_3C-Fe/NC-800). A reasonable range of EXAFS fitting parameters: $0.700 < S_0^2 < 1.000$; $CN > 0$; $\sigma^2 > 0$ Å^2; $|\Delta E_0| < 15$ eV; *R* factor < 0.02.

Table S4 $E_{1/2}$, overpotential and Tafel slopes of the prepared catalysts, Pt/C and RuO_2.

Sample	$E_{1/2}$ /V	Tafel slope$_{ORR}$ /mV dec^{-1}	Overpotantial$_{OER}$ /mV	Tafel slope$_{OER}$ /mV dec^{-1}	Overpotantial$_{HER}$ /mV	Tafel slope$_{HER}$ /mV dec^{-1}
Fe_3C-Fe/NC-800	0.86	69	230	80.1	124	56.6
HM-800	0.66	141	321	93.8	297	64.9
SiO_2	0.42	281	-	-	-	-
Pt/C	0.85	90	-	-	62	33.9
RuO_2	-	-	316	125.7	-	-

Table S5 Simulated R_s and R_{ct} value of Fe_3C-Fe/NC-800, RuO_2 and HM-800 for OER.

Sample	R_s/Ω	R_{ct}/Ω
Fe_3C-Fe/NC-800	1.74	1.62
HM-800	1.61	3.74
RuO_2	2.11	13.95

Table S6 Simulated R_s and R_{ct} value of Fe_3C-Fe/NC-800, Pt/C and HM-800 for HER.

Sample	R_s/Ω	R_{ct}/Ω
Fe_3C-Fe/NC-800	1.87	3.69
HM-800	1.68	8.69
Pt/C	1.60	0.85

Table S7 Summary of ORR, OER and HER performances of reported multifunctional electrocatalysts in recent open literatures.

Catalyst	ORR				OER	HER	Ref.
	$E_{1/2}$/V	J/mA cm^{-2}	J loss of Catalyst/%	time/h	η_1/mV	η_2/mV	
Fe_3C-Fe/NC-800	0.86	6.05	14	15	221	124	This work
GO-PANi-FP	0.72	-	-	-	587	520	[8]
Fe_3C-Co/NC	0.88	5.50	-	16	340	238	[9]
Fe-N_4 SAs/NPC	0.88	5.50	-	-	430	202	[10]
Fe@CN_x	0.84	4.4	14	2.77	410	460	[11]
Co/CNT/MCP-850	0.80	4.8	-	-	270	110	[12]
Co-N-S-C	0.82	5.1	5	2.77	400	264	[13]
Co@N-CNTF-2	0.81	5.2	7.7	9.72	350	220	[14]
Co_9S_8@Co_9S_8@MoS_2-0.5	0.78	4.76	11	12	340	173	[15]
M-NC-CoCu	0.75	4.9	10	19.4	310	240	[16]
Co_2P/CoNPC	0.84	5.4	-	-	326	208	[17]
Mo-N/C@MoS_2	0.81	5.3	8.2	16	390	117	[18]
Ni_xCo_{1-x}@Ni_xCo_xONCNT	0.79	5.29	-	-	380	68	[19]
Co_9S_8@MoS_2	0.884	3	-	10	342	143	[20]
FeCo/Co_2P@NPCF	-	5.3	3	12	330	260	[21]
Pt@CoS_2-NrGO	0.85	6	-	-	235	39	[22]

$Co_{0.85}Se$@NC	0.817	3.6	14.8	10	320	230	[23]
NCNT/Ni-$NiFe_2O_4$	0.59	-	12	6	250	38	[24]
Pt_{SA}-PtCoNCs/NCNT-900	0.86	5.2	3.9	2.77	252	47	[25]
Co_9S_8-MoS_2/N-CNAs@CNFS	0.82	5.3	14	11.11	340	163	[26]

Table S8 Total number of spectra of distribution maps before HER stability test.

Elemental	wt%	wt% Sigma	At%
C	48.28	0.29	74.13
N	0.88	0.21	1.16
O	9.63	0.10	11.10
Fe	41.21	0.32	13.61
Overall amount	100.00		100.00

Table S9 Total number of spectra of distribution maps after HER stability test.

Elemental	wt%	wt% Sigma	At%
C	52.15	0.33	77.12
N	1.45	0.23	1.84
O	7.92	0.09	8.80
Fe	38.43	0.36	12.24
Overall amount	100.00		100.00

Table S10 Comparison of the performance of Fe_3C-Fe/NC-800 with other reported catalysts for Zn-air batteries.

Catalyst	Open circuit voltage /V	Specific capacity /mA h g^{-1}	Ref.
Fe_3C-Fe/NC-800	1.46	813	This work
Fe-Nx/Fe_3C@NC	1.40	705	[27]
Co2P/CoNPC	1.425	-	[28]
Co_4N@NC-2	1.48	769.4	[29]
Co_4NC@NC	1.38	759.6	[30]
Co-N-S-C	1.44	-	[13]
FeCo/Co_2P@NPCF	1.44	-	[21]
NCNT/Ni-$NiMn_2O_4$	1.2	502	[24]
3D Fe-S, N-C	1.44	817	[31]
Fe-S, N-C-950	1.459	660	[32]
Fe_3C–FeN/NC-2	1.41	745	[33]
FeCo-N-C-700	1.39	518	[34]

Table S11 Comparison of the performance of Fe_3C-Fe/NC-800 with other reported catalysts for overall water splitting.

Catalyst	Open circuit voltage /V	Current density (mA cm^{-2})	Ref.
Fe_3C-Fe/NC-800	1.70	10	This work
Fe_3C-Co/NC	1.77	10	[9]
Co_9S_8@MoS_2	1.67	10	[20]
FeCo/Co_2P@NPCF	1.68	10	[21]
$Co_{0.85}$Se@NC	1.76	10	[23]
CoS_x/NCS	1.83	10	[35]
3D-CNTA	1.68	10	[36]
FeNiP/NPCS	1.71	10	[37]
Fe_2P/Co@NPC	1.73	10	[38]
Co@NCL	1.70	10	[39]
Ir@NG-750	1.70	10	[40]

Table S12 ΔG of ORR from DFT calculations.

Reaction	$\Delta G_{Fe3C/Fe-N4}$/eV	ΔG_{Fe-N4} /eV	ΔG_{Fe3C}/eV
$* + O_2\,(g) + H_2O\,(l) + e^- \rightarrow *OOH + OH^-$	-0.158	-1.020	-0.973
$*OOH + e^- \rightarrow *O + OH^-$	-0.683	-1.054	-2.973
$*O + H_2O\,(l) + e^- \rightarrow *OH + OH^-$	-0.692	-0.186	0.970
$*OH + e^- \rightarrow * + OH^-$	-0.078	0.694	1.366

Reference

1. G. Kresse and J. Hafner, *Physical Review B Condensed Matter*, 1993, **47**, 558-561.
2. G. Kresse and J. Furthmüller, *Physical Review B*, 1996, **54**, 11169.
3. J. P. Perdew, K. Burke and M. Ernzerhof, *American Physical Society*, 1996, 3865.
4. P. Blochl, E. Blöchl and P. Blöchl, 1994, **50**, 17953.
5. J. K. NoRskov, J. Rossmeisl, A. Logadottir, L. Lindqvist, J. R. Kitchin, T. Bligaard and H. Jónsson, *Journal of Physical Chemistry B*, 2004, **108**, 17886-17892.
6. G. L. Tian, Q. Zhang, B. Zhang, Y. G. Jin, J. Q. Huang, D. S. Su and F. Wei, *Advanced Functional Materials*, 2014, **24**, 5956-5961.
7. T. Wang, C. Yang, Y. Liu, M. Yang, X. Li, Y. He, H. Li, H. Chen and Z. Lin, *Nano Letters*, 2020, **20**, 5639-5645.
8. J. Zhang and L. Dai, *Angewandte Chemie Internation Edition*, 2016, **55**, 13296-13300.
9. C. C. Yang, S. F. Zai, Y. T. Zhou, L. Du and Q. Jiang, *Advanced Functional Materials*, 2019, **27**, 1901949-1901949.
10. Y. Pan, S. Liu, K. Sun, X. Chen, B. Wang, K. Wu, X. Cao, W. C. Cheong, R. Shen, A. Han, Z. Chen, L. Zheng, J. Luo, Y. Lin, Y. Liu, D. Wang, Q. Peng, Q. Zhang, C. Chen and Y. Li, *Angewandte Chemie International Edition*, 2018, **57**, 8614-8618.
11. J. Quílez-Bermejo, S. García-Dalí, A. Daouli, A. Zitolo, R. L. S. Canevesi, M. Emo, M. T. Izquierdo, M. Badawi, A. Celzard and V. Fierro, *Advanced Functional Materials*, 2023.
12. X. Zhou, X. Liu, J. Zhang, C. Zhang, S. J. Yoo, J.-G. Kim, X. Chu, C. Song, P. Wang, Z. Zhao, D. Li, W. Zhang and W. Zheng, *Carbon*, 2020, **166**, 284-290.
13. J. Chen, L. Qiu, Z. Li, G. Gao, W. Zhong, P. Zhang, Y. Gong and L. Deng, *Electrochimica Acta*, 2019, **304**, 350-359.
14. H. Guo, Q. Feng, J. Zhu, J. Xu, Q. Li, S. Liu, K. Xu, C. Zhang and T. Liu, *Journal of Materials Chemistry A*, 2019, **7**, 3664-3672.
15. J. Li, G. Li, J. Wang, C. Xue, X. Li, S. Wang, B. Han, M. Yang and L. Li, *Inorganic Chemistry Frontiers*, 2020, **7**, 191-197.
16. A. Macedo Andrade, Z. Liu, S. Grewal, A. J. Nelson, Z. Nasef, G. Diaz and M. H. Lee, *Dalton Transactions*, 2021, **50**, 5473-5482.
17. H. Liu, J. Guan, S. Yang, Y. Yu, R. Shao, Z. Zhang, M. Dou, F. Wang and Q. Xu, *Advanced Materials*, 2020, **32**, e2003649.
18. I. S. Amiinu, Z. Pu, X. Liu, K. A. Owusu, H. G. R. Monestel, F. O. Boakye, H. Zhang and S. Mu, *Advanced Functional Materials*, 2017, **27**.
19. R. Jena, S. Bhattacharyya, N. Bothra, V. Kashyap, S. K. Pati and T. K. Maji, *ACS Applied Materials & Interfaces*, 2023, **15**, 27893-27904.
20. J. Bai, T. Meng, D. Guo, S. Wang, B. Mao and M. Cao, *ACS Applied Materials & Interfaces*, 2018, **10**, 1678-1689.
21. Q. Shi, Q. Liu, Y. Ma, Z. Fang, Z. Liang, G. Shao, B. Tang, W. Yang, L. Qin and X. Fang, *Advanced Energy Materials*, 2020, **10**.
22. N. Logeshwaran, S. Ramakrishnan, S. S. Chandrasekaran, M. Vinothkannan, A. R. Kim, S. Sengodan, D. B. Velusamy, P. Varadhan, J.-H. He and D. J. Yoo, *Applied Catalysis B: Environmental*, 2021, **297**.
23. T. Meng, J. Qin, S. Wang, D. Zhao, B. Mao and M. Cao, *Journal of Materials Chemistry A*, 2017, **5**, 7001-7014.
24. Q. Qin, L. Chen, T. Wei, Y. Wang and X. Liu, *Catalysis Science & Technology*, 2019, **9**, 1595-1601.
25. W. Chen, X. Zhu, W. Wei, H. Chen, T. Dong, R. Wang, M. Liu, K. Ostrikov, P. Peng and S. Q. Zang, *Small*, 2023, **19**.
26. W. Zhang, X. Zhao, Y. Zhao, J. Zhang, X. Li, L. Fang and L. Li, *ACS Applied Materials & Interfaces*, 2020, **12**, 10280-10290.
27. C. Xu, L. Chen, Y. Wen, S. Qin, H. Li, Z. Hou, Z. Huang, H. Zhou and Y. Kuang, *Materials Today Energy*, 2021, **21**, 100721.
28. H. Liu, J. Guan, S. Yang, Y. Yu, R. Shao, Z. Zhang, M. Dou, F. Wang and Q. Xu, *Advanced Materials*, 2020, **32**.
29. H. Ge, G. Li, J. Shen, W. Ma, X. Meng and L. Xu, *Applied Catalysis B: Environmental*, 2020, **275**.
30. G. Zhang, L. Zhao, G. Li and L. Xu, *Journal of Materials Chemistry A*, 2023, **11**, 11712-11720.
31. Z. Yang, J. Gao, S. Liu, P. Zhu, S. Huang, D. Zeng, X. Zhao and G. Wang, *Electrochimica Acta*, 2020, **364**, 137301.

32. H. Xu, D. Wang, P. Yang, A. Liu, R. Li, L. Xiao, J. Zhang, Z. Qu and M. An, *Sustainable Energy & Fuels*, 2021, **5**, 2695-2703.
33. F. Zhou, P. Yu‡, F. Sun, G. Zhang, X. Liu and L. Wang, *Journal of Materials Chemistry A*, 2021, **9**, 6831-6840.
34. X. Duan, S. Ren, N. Pan, M. Zhang and H. Zheng, *Journal of Materials Chemistry A*, 2020, **8**, 9355-9363.
35. Q. Ju, R. Ma, Y. Pei, B. Guo, Q. Liu, T. Zhang, M. Yang and J. Wang, *Materials Research Bulletin*, 2020, **125**.
36. S. Wang, J. Qin, T. Meng and M. Cao, *Nano Energy*, 2017, **39**, 626-638.
37. J.-T. Ren, Y.-S. Wang, L. Chen, L.-J. Gao, W.-W. Tian and Z.-Y. Yuan, *Chemical Engineering Journal*, 2020, **389**.
38. Y. Bai, Y. Wang, Z. Qiao, Y. Yang, L. Deng, C. Li, X. Chen, S. Wang, Y. Huang, X. Zhang and D. Cao, *Journal of Materials Chemistry A*, 2022, **10**, 16037-16045.
39. Q. Liu, Q. Shi, Y. Ma, Z. Fang, Z. Zhou, G. Shao, H. Liu and W. Yang, *Chemical Engineering Journal*, 2021, **423**.
40. Q. Zhang, Z. Duan, Y. Wang, L. Li, B. Nan and J. Guan, *Journal of Materials Chemistry A*, 2020, **8**, 19665-19673.